\$50 COLUMN SELSEVIER

Contents lists available at ScienceDirect

Computational Materials Science

journal homepage: www.elsevier.com/locate/commatsci





Development of a 2NN-MEAM potential for Ti–B system and studies of the temperature dependence of the nanohardness of TiB₂

Siamak Attarian*, Shaoping Xiao

Department of Mechanical Engineering, University of Iowa Technology Institute, The University of Iowa, Iowa City, IA, 52242, USA

ARTICLE INFO

Dataset link: https://doi.org/10.17632/gy97bcv4dm.2

Keywords: Interatomic potential Titanium boride Molecular dynamics Nanohardness Nanoindentation Ceramic

ABSTRACT

Boride ceramics are materials of choice in extreme conditions. Among them, titanium borides have many applications due to their high hardnesses and melting points. The behavior of titanium borides may not be easily studied at very high pressures and temperatures by experimental means. Alternatively, molecular dynamics (MD) is a powerful computational tool to investigate the desired behavior of materials in certain conditions. In this study, we develop an interatomic potential for the Ti–B system based on the second nearest-neighbor modified embedded atom method (2NN-MEAM) formulation. With the developed potential, MD simulations reproduce many physical, mechanical, and thermal properties of titanium borides with good accuracy. As an application of the developed potential, a series of nanoindentation simulations is also conducted to investigate the temperature dependence of the nanohardness of TiB₂ up to 1500 K. The results illustrate a linear dependence between nanohardness and temperature.

1. Introduction

Metal matrix borides have many properties, such as high melting point, elastic modulus, hardness, and thermal conductivity, that make them interesting for technological applications [1]. Among these compounds, titanium borides have been the focus of increasing interest in recent years [2,3]. The Ti-B phase diagram has three compounds [4] TiB, TiB2, and an intermediate compound, Ti3B4. TiB is usually produced by the in situ reaction between Ti and TiB2 particles, and the resulting metal-ceramic composite (Ti/TiB) has many current and prospective applications in the automotive, aerospace, and biomedical industries [5,6]. TiB2 is an ultra-high-temperature ceramic that is used in impact-resistant armors [7], cutting tools [8], and crucibles [9], and due to its good electrical conductivity, it is also used as an electrode [10]. One of the recent promising applications of TiB₂ is to use it as a coating on other materials [11-13]. Due to the importance of the hardness of TiB2 coatings and thin films, several studies have been focused on testing the nanohardness of TiB2 films, and a range of values from 28 GPa to 73 GPa have been reported [14-21]. These experiments differed in many factors including the deposition method of the TiB2 layer, deposition variables such as temperature and negative bias voltage, microstructure, and texture of the deposited TiB2. Most of these experimental studies were limited to room temperature, but many of the intended applications of TiB₂ are at high temperatures. Therefore, it is necessary to investigate the properties of TiB2 at higher temperatures, up to 1500 K (the maximum temperature), at which TiB₂ can operate well in oxidizing atmospheres [14].

An alternative way to investigate the properties of materials at conditions inaccessible to experimental studies is with molecular dynamics (MD) simulations. Nanoindentation simulations have been performed on many materials with comparable results to experimental studies. Abdeslam [22] investigated the influence of silver inclusion on the mechanical behavior of Cu-Ag nanocomposites using nanoindentation simulation. Xiang et al. [23] studied the orientation dependence of deformation in monocrystalline AlN during nanoindentation simulation. Patil et al. [24] studied the mechanical properties and deformation behavior of nanoporous silica aerogels by means of nanoindentation simulations, and Zhao et al. [25] conducted nanoindentation simulations to study the temperature-dependent mechanical properties of MoS₂.

To perform MD simulations, interatomic potentials between all the atoms involved in the simulation are required. There are many unary interatomic potentials for titanium reported in the literature, including the embedded atom method (EAM) [26], the second nearest-neighbor modified embedded atom method (2NN-MEAM) [27], and the charge-optimized many-body (COMB3) potential [28]. In addition, several binary potentials such as Ti–Al [29], Ti–C [28], and Ti–O [30] have been developed. However, the potential functions for boron are rare and only parametrized for specific binary systems, e.g., B–N [31–33].

E-mail address: siamak-attarian@uiowa.edu (S. Attarian).

^{*} Corresponding author.

To simulate compounds such as TiB_2 , where $\mathrm{Ti-Ti}$, $\mathrm{Ti-B}$, and $\mathrm{B-B}$ bonds exist, interatomic potentials for all three combinations are needed. In a recent article [34], we discussed the difficulties in developing an interatomic potential for boron according to the currently available potential formulations and reviewed several available potentials for boron with their shortcomings. We also developed a new potential for boron, based on the 2NN-MEAM [35] formulation. Although the developed potential successfully reproduces the mechanical and thermal properties of boron polymorphs, we had difficulties in extending it to a binary potential for $\mathrm{Ti-B}$.

This study aims to develop an interatomic potential for the Ti–B system based on the 2NN-MEAM formulation, including a new parameter set for B–B to be functional within the Ti–B system. In Section 2, the procedure of choosing and fitting the interatomic potential is reviewed. In Section 3, the potential is implemented in MD simulations to calculate the mechanical and thermal properties of various titanium borides, which are compared with the experimental or density functional theory (DFT) results. Section 4 presents an application of the developed potential by performing nanoindentation simulations to obtain the nanohardness of TiB $_2$ at various temperatures, and Section 5 presents conclusions.

2. Potential development

2.1. 2NN-MEAM potential function

Fig. 1 shows the unit cells of TiB-B27 (which for simplicity will be referred to as TiB), TiB2, and Ti3B4. The Ti-B bonds in all three compounds are covalent with partial ionicities [36]; the B-B bonds are covalent, and the Ti-Ti bonds are metallic. To develop an interatomic potential function, a proper formalism should be chosen based on the bonding nature of the material in focus. At first, we tried to build the potential based on the COMB3 formulation [37], which already has a developed Ti-Ti potential [38] and is known to be more suitable for compounds with multiple bonding natures. However, our efforts to develop a potential for the B-B bond were unsuccessful. Since the 2NN-MEAM formulation worked well for B–B bonding in boron polymorphs in our previous study [34], and it has also performed well for other similar ceramics such as TiN or TiC [39], we chose 2NN-MEAM for this research. To account for the ionicity, we also considered 2NN-MEAM+Qeq [40], but the results were not noticeably better than the regular 2NN-MEAM except for higher run times. Therefore, we proceeded with the regular 2NN-MEAM.

The total energy of a unary system in the 2NN-MEAM formalism is calculated by:

$$E = \sum_{i} [F(\bar{\rho}_i) + \frac{1}{2} \sum_{j(\neq i)} \phi(R_{ij})]$$
 (1)

where F is the embedding function, which calculates the amount of energy needed to embed an atom of type i in the background electron density $\bar{\rho_i}$. $\bar{\rho_i}$ can be obtained based on the partial background electron densities $\rho_i^0 \sim \rho_i^3$, which are functions of the relative position of atoms within the cut-off radius from atom i. $\phi(R_{ij})$ is the pair interaction between atoms i and j by a distance R_{ij} , which depends on the Rose energy function [41]. The 2NN-MEAM formulation has been described extensively in the literature, and readers are referred to the original papers [35,42] for detailed information. Overall, there are 14 adjustable parameters in unary 2NN-MEAM: " β^0 ", " β^1 ", " β^2 ", " β^3 ", " t^1 ", " t^2 ", and " t^3 " are used to calculate the partial background electron densities; "A" is used in the embedding function formulation; " E_c ", " R_e ", " α ", and " α " are part of the Rose energy function; and " α 0" and " α 0" are screening parameters for the second nearest neighbors.

For binary systems, the 2NN-MEAM has a similar form and includes all the energy contributions from type i and type j atoms and their interactions. It has 13 adjustable parameters: " ρ_i^0 : ρ_j^0 " accounts for the ratio between the zeroth partial background electron density of

type i atom and type j atom; " E_c ", " R_c ", " α ", and "d" are used for the pairwise interaction between atoms i and j; and eight screening parameters (four pairs of C_{min} and C_{max} for Ti–B–B, Ti–Ti–B, B–Ti–B, and Ti–B–Ti).

Besides the above-mentioned parameters, the 2NN-MEAM is formulated based on a few reference structures. Some parameters such as the number of the nearest neighbors, their relative position, etc., are set in the formulation based on the selected reference structure. For unary systems the conventional structures (fcc, bcc, hcp, diamond, or dimer) are available and for binary systems, a few structures such as NaCl type, CsCl type, etc. can be selected.

2.2. Parameter fitting

There are a total of 27 parameters to be fit (14 for boron unary potential and 13 for Ti-B binary potential). Ideally, the task of optimizing the unary and binary potentials could be done separately. However, as we mentioned in Section 1, our previously developed unary potential for boron did not help us to further fit potential parameters for Ti-B that would reproduce acceptable results for titanium borides. Therefore, we fitted all of 27 parameters simultaneously through the optimization procedure developed in this work. The main goal of the potential parametrization was to reproduce the physical and mechanical properties of titanium borides. For a better approximation of the interatomic interaction of B-B bonds, we also considered the energies of a series of stable molecular structures of boron as done previously by other authors to develop the potentials for other compounds of boron [31,43]. The selected structures, shown in Fig. 2, consist of α -B and β -B, which are stable polymorphs of boron in ambient conditions, and a few nanoclusters and nanosheets of boron that have been shown to be stable in previous studies [44–47].

To parameterize the 2NN-MEAM, an optimization procedure was carried out with the following objective function:

$$P = \sum_{i}^{n} w_{i} \left| \frac{A_{i}^{M} - A_{i}^{D}}{A_{i}^{D}} \right| \tag{2}$$

where n is the number of objectives, w_i is the weight coefficient of objective i, A_i^M is the physical or material property i resulting from MD simulations with the developed potential, and A_i^D is the same property obtained from DFT calculations. Overall, 32 physical and material properties were used in the objective function: 3 lattice constants of TiB, 2 lattice constants of TiB2, formation energies of TiB and TiB2, 9 elastic constants of TiB, 5 elastic constants of TiB2, 2 lattice constants of α -B and 9 cohesive energies of the boron structures presented in Tables 2 and 3.

In each optimization iteration, the physical and material properties were evaluated after MD simulations. At first, the energies and the lattice constants of TiB and TiB $_2$ were derived after full relaxation of the unit cell and atomic positions. Then, the elastic constants were calculated by deforming the relaxed unit cell with 0.5% and -0.5% strains in different directions (normal and shear deformations), further relaxing the atomic positions of the unit cell and measuring the stress, and finally averaging the results. In addition, the energy and lattice constants of $\alpha\text{-B}$ were derived after full relaxation of the unit cell and atomic positions. The energies of the other boron structures were derived in their original configurations without relaxation.

Since A_i^M in (2) were calculated from MD simulations, the objective function did not have an explicit form so the derivative-based optimization methods could not be used for this problem, and we needed to use a derivative-free algorithm as was done in other works [48]. Guided by the no free lunch theorem [49] that states there is no single optimization algorithm that performs the best in every problem, we tried several optimization algorithms and assessed their performances on this problem.

First, we considered multi-objective approaches based on the Pareto optimality where the objective function was calculated for each objective separately without the summation. We used the non-dominated

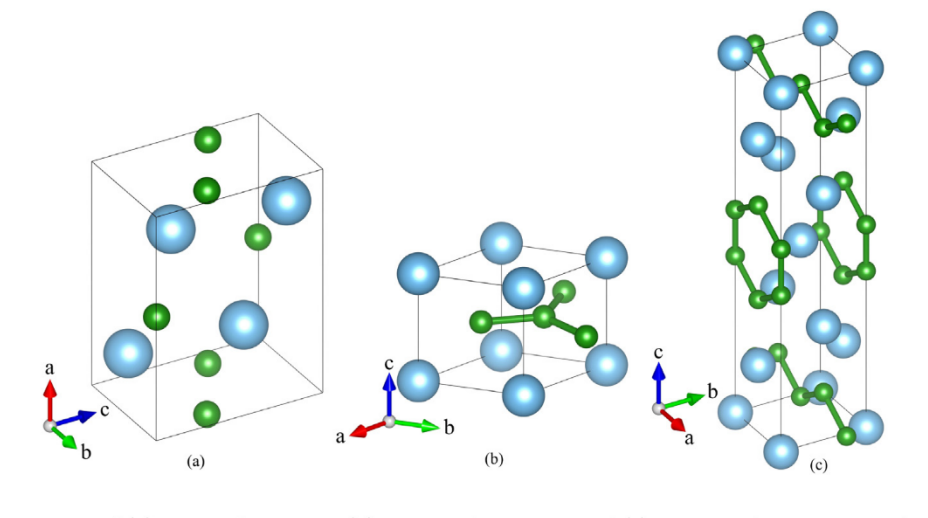


Fig. 1. Crystal structures of (a) TiB with 8 atoms, (b) TiB_2 with 3 atoms, and (c) Ti_3B_4 with 14 atoms in their respective unit cells. Some of the atoms at the edges of TiB_2 and Ti_3B_4 belong to the neighboring unit cells. Blue atoms represent titanium, and green atoms represent boron.

sorting genetic algorithm II [50] which is a well-established optimization algorithm. Because of the multitude of the objectives, every offspring within the population became non-dominated and was considered as a Pareto optimal solution after a few generations. Therefore, such an approach did not generate useful results. Decreasing the number of the objectives by combining them in groups did not help either.

Next, we used a single objective function based on the weighted sum of the normalized errors of each objective as is presented in (2). Among many available swarm-based global optimization algorithms, we tried the original particle swarm optimization (PSO) [51], quantum particle swarm optimization (QPSO) [52], gray wolf optimizer (GWO) [53], firefly algorithm [54], and one algorithm based on the evolutionary strategies (CMA-ES [55]). Overall, the PSO, QPSO, and GWO did not perform well compared to the firefly algorithm in finding high-quality solutions within the same number of iterations. CMA-ES showed a considerably fast convergence rate (under 100 iterations) but it would mostly converge to the same solution in each run with the loss of diversity. On the other hand, the firefly algorithm showed a good performance in exploring the search space and provided a different solution in each run although it was slow and mostly converged somewhere between 1000 to 1500 iterations. The convergence was deemed to be achieved when there were no improvements after 100 iterations. Both firefly algorithm and CMA-ES have a time complexity of $O(n^2)$ where n is the population size. Based on these observations we proposed the following 4-step strategy to develop the 2NN-MEAM potential functions in this study:

- 1. The firefly algorithm was used at the beginning of the optimization where the search space is wide to find different possible regions for optimal solutions
- 2. After narrowing down the search space to a couple of regions, CMA-ES was used to find the optimum in each selected region.
- 3. Steps 1 and 2 were repeated many times, and many local optima were recorded. Each of these solutions was examined to obtain the material properties of ${\rm Ti}_3{\rm B}_4$, which were not considered in the main objective function in (2). The solutions that reproduced acceptable results were kept.
- 4. The solution candidates from Step 3 were used in MD simulations to calculate the thermal properties of ${\rm TiB_2}$ that were not considered in the main objective function either. The best performing solution was selected as the final solution.

Such a procedure ensures that out of the many possible local minima that the optimization algorithm finds, the one that has more predictability power is chosen. As can be seen in Tables 4 and 5, the

derived potentials have been also used to calculate the material properties of TiB–B $_f$ and the thermal properties and the surface energies of TiB to assess its performance.

Choosing the initial bounds of the search space was also carried out differently for different parameters. The first step in developing a 2NN-MEAM potential is choosing a reference structure. If the reference structure is a stable phase of the element, the parameters E_c and R_e become the cohesive energy and the nearest neighbor distance of the atoms in the reference structure. The parameter α is then calculated via $\alpha = \sqrt{9B\Omega/E_c}$, where B is the bulk modulus of the element and Ω is the atomic volume. Since neither boron nor any of the Ti-B ceramics have a crystal structure for which the 2NN-MEAM algorithm has a special treatment, we chose fcc as the reference structure for boron and B1 structure, i.e., NaCl type, for Ti-B. Then, by performing several DFT simulations, we obtained the parameters E_c , R_e , and B(and subsequently α) for boron and TiB in their respective reference structures. The obtained values were used to set the initial ranges for the aforementioned parameters. For the rest of the parameters, we chose initial bounds based on the developed 2NN-MEAM potential functions for other materials available in the literature [29,39,56].

Although all the material properties were affected by changes in each parameter, some material properties were more sensitive to some parameters than the others. Based on our simulations, the cohesive energies of borons were mostly affected by changing \mathbf{E}_c , \mathbf{R}_e , β_0 and A of the unary potential. The formation energies of Ti–B ceramics were mostly affected by changing \mathbf{E}_c and \mathbf{R}_e of both unary and binary potentials. The elastic constants were mostly affected by the changes in α of both unary and binary potentials. On the other hand, the material properties were less sensitive to the values of \mathbf{t}_1 , \mathbf{t}_2 , \mathbf{t}_3 and the screening parameters (\mathbf{C}_{max} and \mathbf{C}_{min}) of both unary and binary potentials.

The weight coefficients were initially set to 1 for all the objectives, but by observing the errors of the objectives during the optimization these weights were adjusted. For instance, we observed that in many regions of the search space the material properties of ${\rm TiB_2}$ can be reproduced correctly while the situation was not the same for the material properties of TiB. Therefore, the weight coefficients for the material properties of TiB were set to higher values, so the optimization algorithm would mostly explore the regions of the search space that agreed with TiB. The off-diagonal elements of the elastic tensors of both TiB and ${\rm TiB_2}$ were somewhat inconsistent with the rest of the objectives during the optimization. It was observed that when the optimization algorithm tries to decrease their errors at the beginning of the optimization, it would result in high errors for the other objectives. Lowering their weight coefficients would help the optimization

Table 1
The 2NN-MEAM parameters of boron (B) developed in this work and titanium (Ti) [27]. The reference structure for boron and titanium are fcc and hcp, respectively. A cutoff radius of 5 Å is used.

	α	E_c	R_e	\boldsymbol{A}	β^0	β^1	β^2	β^3	t^1	t^2	t^3	d	C_{min}	C_{max}
В	5.407	5.734	1.86	1.843	0.424	0.024	-0.803	1.418	16.255	4.521	-11.674	0	0.164	2.377
Ti	4.718	4.87	2.92	0.66	2.70	1.00	3.00	1.00	6.80	-2.00	-12.00	0	1.00	1.44

Table 2
Comparison of the energies (eV/atom) and lattice constants (Å) of boron structures (shown in Fig. 2) obtained from MD and DFT. The energies from DFT are rescaled based on the formation energy of boron from experimental studies [57].

	Energy from MD unrelaxed, relaxed	Rescaled target energy from DFT	Relaxed lattice constants from MD	Lattice constant from DFT
α-В	-5.650, -5.872	-5.858	a = 4.9,	a = 4.9,
			c = 12.55	c = 12.55
β-B	-6.014, -6.091	-5.832	a = 11.10,	a = 10.92,
			c = 23.82	c = 23.75
Nano sheet (c)	-5.421, -5.687	-5.457	_	_
Nano sheet (d)	-5.442, -5.716	-5.443	_	-
Cluster (e)	-5.134, -5.538	-5.186	_	-
Cluster (f)	-5.123, -5.597	-5.174	_	_
Cluster (g)	-5.175, -5.490	-5.143	_	-
Cluster (h)	-5.176, -5.551	-5.122	_	-
B ₈₀ (i)	-5.428, -5.676	-5.280	-	-

algorithm to efficiently locate the optimal regions of the search space. The energies of borons and titanium borides were not sensitive to their weight coefficients, so their weight coefficients were kept unchanged.

The DFT calculations to obtain the objectives were performed using Quantum ESPRESSO code [58] and the projector-augmented wave (PAW) [59] method within the generalized gradient approximation of Perdew-Burke-Ernzerhof (PBE-GGA) [60] for the exchange and correlation functional. A cutoff energy of 585 eV (43 Ry) for the plane-wave basis set was used. For boron structures a k-point mesh of $8 \times 8 \times 8$ and for titanium borides a k-point mesh of $12 \times 12 \times 12$ was chosen to sample the Brillouin zone. To calculate the energy of a single isolated atom, we used spin polarization. The elastic constants were calculated based on the stresses of fully relaxed unit cells deformed in different directions by 0.5% strain. Since the cohesive energies obtained from DFT calculations are usually different than experimental results, we rescaled all the energies based on the most recent formation energy obtained for boron [57] and used the rescaled values as optimization targets. Such corrections are common when developing interatomic potentials [61,62]. LAMMPS code [63] was used for MD simulations, and Vesta [64] and OVITO [65] were used for graphical representations.

3. Potential validation

3.1. Borons

Table 1 shows the parameters of the 2NN-MEAM potential developed in this work for boron. The parameters developed by Kim et al. [27] for titanium are also listed in Table 1.

Table 2 compares the energies of boron structures (shown in Fig. 2) obtained from MD simulation using the developed potential with the energies obtained from DFT calculations. All the DFT values are for relaxed structures. It shall be noted that α -B is assumed to be the most stable structure of boron. Since the cohesive energy of α -B is used to calculate the formation energy of titanium borides, it is important to predict the lattice constants and cohesive energy of relaxed α -B with good accuracy.

3.2. Ti-B Compounds

Table 3 lists the developed 2NN-MEAM parameters for the Ti–B system, and Table 4 presents the physical, mechanical, and thermal properties of TiB and ${\rm TiB_2}$ calculated by the MD simulation using the developed potential. The results are compared with the experimental and DFT results, if available, as shown in Table 4. The bulk

modulus is calculated by fitting the parameters of the third-order Birch–Murnaghan equation [66] using pressures and volumes of the unit cells that were under hydrostatic strains in the range -5% \sim 5%. The elasticity modulus and Poisson's ratio are obtained based on Hill's approximation [67,68].

To calculate the thermal properties, we used a $10 \times 10 \times 10$ supercell for each ceramic (8000 atoms for TiB and 3000 atoms for TiB₂). NPT simulations at 1 bar were conducted from temperature 0.1 K up to 3500 K. The time step was 1 fs. During the simulations, at each 25 K interval we let the system equilibrate by 30000 steps, and then through another 30000 steps the system moved to the next temperature. The entire duration of each simulation was 4.23 ns. Quantities such as lattice constants and enthalpy were recorded and later averaged at each stationary step (every 25 K). They were used to calculate the thermal expansion coefficients and the specific heat respectively. The linear thermal expansion coefficient is calculated using the following equation:

$$\alpha_l = \frac{l_T - l_{293k}}{l_{293k}(T - 293)} \tag{3}$$

where l_T is the lattice constant at the temperature T. The specific heat $(C_p = \partial H/\partial T)$, where H is the enthalpy, is calculated at temperatures above the Debye temperature. It is because the quantum mechanical effects greatly influence the value of the specific heat at the temperatures below the Debye temperature so that it cannot be captured by MD simulations [69–71] . The melting temperature is calculated as the temperature where the volume has an instantaneous increase during each NPT simulation.

The physical and mechanical properties of TiB are predicted very well as shown in Table 4. The predicted surface energies are within the accuracies obtainable by MD simulations. The thermal expansion of TiB in the a and b directions (see Fig. 1) are reported at temperatures between 293 K and 1500 K and compared with the results of [72]. The specific heat is reported for temperatures between 954 K (its Debye temperature [73]) and 2000 K. The predicted melting point is also close to its actual value. Overall, the thermal properties of TiB calculated via MD simulations agree with the reference values. It is worth mentioning that experimental results for TiB are rare and are mostly obtained by indirect measurements based on Ti/TiB composites.

The physical and mechanical properties of ${\rm TiB_2}$ are also in good agreement with the experiments. We could not find a stoichiometric surface of ${\rm TiB_2}$ to compare the surface energies. The thermal expansion coefficient is calculated at temperatures between 293 K and 2000 K and compared to the experimental results of Fendler et al. [88]. The specific

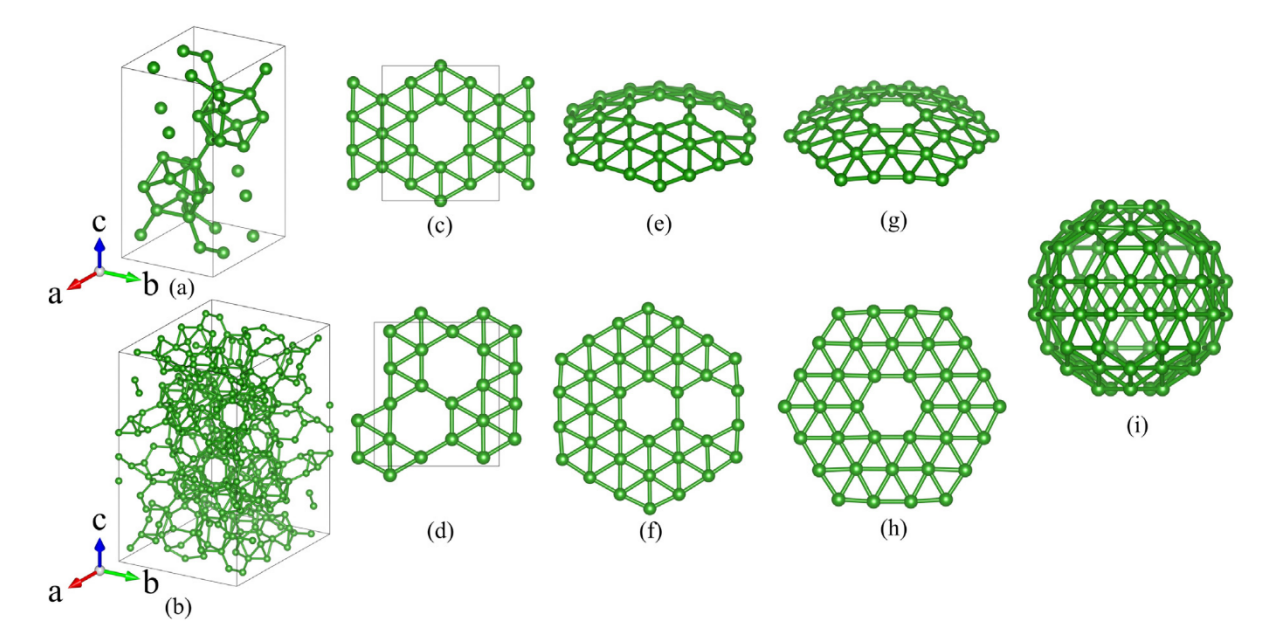


Fig. 2. (a) α -B with 36 atoms, (b) β -B with 315 atoms, (c, d) boron nanosheets with 14 atoms in a unit cell [45], (e, f, g, h) dome-shaped and flat boron clusters with 35 and 36 atoms [44], (i) B_{80} fullerene [46].

Table 3
The 2NN-MEAM parameters for the Ti-B binary system. The reference structure is B1 (NaCl) type.

ρ_i^0 : ρ_i^0	1.737
α	4.173
E_c	5.521
R_c	2.288
d	0
$C_{min}(B,B,Ti)$	1.136
$C_{min}(Ti,Ti,B)$	0.915
$C_{min}(B,Ti,B)$	1.095
$C_{min}(Ti,B,Ti)$	2.0
$C_{max}(B,B,Ti)$	2.311
$C_{max}(Ti,Ti,B)$	2.708
$C_{max}(B,Ti,B)$	3.263
$C_{max}(B,B,Ti)$	2.8

heat is measured at temperatures above its Debye temperature (1204 K [89]) up to 2000 K. Our MD simulation predicted the melting point of ${\rm TiB_2}$ at about 25% below the actual value. Considering the limitation of the 2NN-MEAM, which is mainly formulated for metallic bonding, and the need to fit the potential to predict different properties of different compounds of titanium and boron, such inaccuracies are acceptable. Overall, the thermal properties of ${\rm TiB_2}$ predicted from MD simulations are close to experimental values.

Besides the main titanium borides (TiB and TiB $_2$), we checked the applicability of the potential for other experimentally verified compounds. Table 5 shows the physical and mechanical properties of Ti $_3$ B $_4$ and TiB $_5$ B $_f$. TiB $_5$ (which has a CrB-type structure) is an unstable compound of Ti and B that is produced sporadically as the stacking faults during the in situ production of TiB whiskers (TiB $_5$ P27 whiskers). There are no experimental results for the thermal properties of Ti $_3$ B $_4$ and TiB $_5$ B $_f$ in the literature. As can be seen in Table 5, the potential works quite well for both compounds in calculating the physical and mechanical properties.

4. Nanoindentation simulation

The developed 2NN-MEAM potential is then used in nanoindentation simulations to study the nanohardness of TiB₂. Fig. 3 shows the simulated model of nanoindentation. The indentation is carried out on

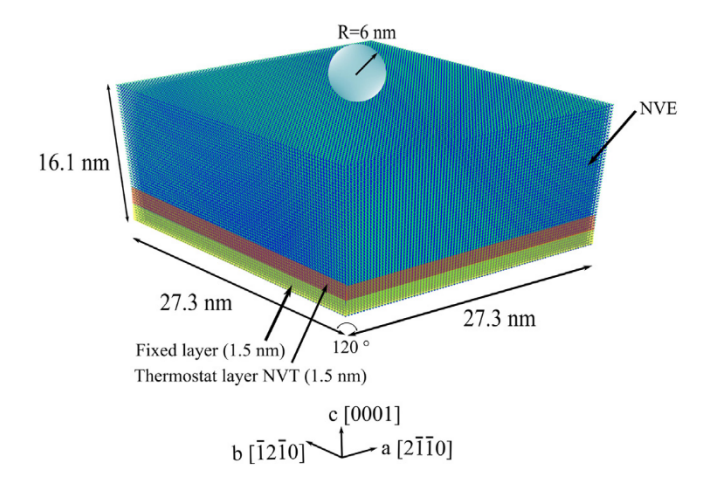


Fig. 3. The simulated model for the nanoindentation.

the (0001) surface, which is the desired direction for the deposition of TiB_2 films [17,90]. The simulation domain is a rhombic prism with an edge length of 27.3 nm (a and b directions in the hexagonal crystal system) and a thickness of 16.1 nm (c direction), and it includes over one million atoms. The domain is periodic in the a and b directions and nonperiodic in c, which is the indentation direction. The bottom layer, with a thickness of 1.5 nm, is fixed to prevent movement of the model during the indentation. A thermostat layer with a thickness of 1.5 nm is used above the fixed layer to dissipate the excessive heat generated by the indentation. The rest of the atoms are modeled with the NVE ensemble. The interaction between the indenter and the atoms of TiB_2 is modeled with a dummy indenter, which exerts a fully repulsive force using the following formula:

$$F(r) = -K(r-R)^2 \quad for \quad r < R; \quad F(r) = 0 \quad for \quad r \ge R$$
(4)

where R is the radius of the indenter, r is the distance of each atom to the center of the indenter, and K is the force constant. The indenter has a radius of R=6 nm, which is large enough to reduce the pileup effect [91]. We use $K=100 \text{ eV/A}^3$ as the force constant, and the effect of the force constant greater than 10 eV/A^3 has been shown to be negligible in nanoindentation simulations [25].

Table 4 Comparison of the mechanical and physical properties of TiB and TiB₂ calculated by MD, DFT, and experimental works. The parameters marked with * have been used in the optimization procedure. a_i , b_i , and c_i are the lattice parameters and are in λ. The formation energies (E_{f}) are in eV/atom, and surface energies (E_{surf}) are in J/m². The bulk moduli (B), elastic constants (C_{ij}), and Young's moduli (E) are in GPa. The melting points (T_m) are in K_i , linear thermal expansion coefficients (α_i) are in (10⁻⁶ K^{-1}), and specific heats (C_p) are in J.(mol. K_i)⁻¹. For calculation of the formation energy, the cohesive energies of hcp titanium and α boron are used.

		2NN-MEAM	DFT (This	Other DFT works	Experimental works	
		(This work)	work)			
TiB	a^*	6.01	6.12	6.11 [72]	6.12 [74]	
	b^*	3.05	3.05	3.05 [72]	3.06 [74]	
	c^*	4.50	4.57	4.57 [72]	4.56 [74]	
	E_f^*	-0.90	-0.83	-0.84 [72], -0.832 [75]	-	
	B	210	209	205.4 [72], 205.5 [76]	-	
	E	433	437	427 [77]	371 [78], 450 [79], 406 [80]	
	G	187	190	-	140 [78]	
	v	0.16	0.14	0.15 [77]	0.16 [78], 0.16 [80]	
	C_{11}^*	394	417	420 [72]	_	
		512	518	517.8 [72]	_	
	C_{22}^{*2}	408	415	412.7 [72]	_	
	C_{44}^{*}	204	196	197.7 [72]	_	
	$C_{\epsilon\epsilon}^{44}$	171	180	178.8 [72]	_	
	$C^*_{22} \ C^*_{33} \ C^*_{44} \ C^*_{55} \ C^*_{66}$	231	222	222.7 [72]	_	
	C_{12}^{*}	89	90	85.5 [72]	_	
	C_{13}^{12}	105	110	103.3 [72]	_	
	C_{23}^{*}	100	60	60 [72]	_	
	$E_{surf}(100)$	3.99	4.51	4.43 [81]	_	
	B terminated	0.55	1.01	1.10 [01]		
	$E_{surf}(100)$	3.94	3.53	3.52 [81]	_	
	Ti terminated	4.00	0.05	0.00 [01]		
	$E_{surf}(001)$	4.23	2.95	2.93 [81]	-	
	α_a	9~12.0	-	8.7~10.9 [72]	-	
	α_b	9~11.2	-	7.0~8.8 [72]	- 50 [00]	
	C_p	50~57	-	_	51~53 [82]	
	T_m	2660		_	2463 [83]	
$\Gamma i B_2$	a^*	3.05	3.03	3.03 [72]	3.038 [84]	
	c^*	3.18	3.23	3.22 [72]	3.239 [84]	
	E_f^*	-1.01	-1.06	-1.07 [72], -1.056 [75]	-1.11 [85]	
	B	256	254	253.7 [72], 256 [75]	250 [84]	
	E	554	580	_	585 [80], 565 [86]	
	G	238	258	-	255 [86]	
	ν	0.17	0.12 –		0.108 [86]	
	C_{11}^*	659	653 654 [72]		660 [87], 654.5 [84]	
	C_{33}^{11}	473	453	459 [72]	432 [87], 454.5 [84]	
	C_{44}^{*}	217	260	258.1 [72]	260 [87], 263.2 [84]	
	C_{12}^{*}	56	64	64.2 [72]	48 [87], 56.5 [84]	
	C_{13}^*	148	104	96.9 [72]	93 [87], 98.4 [84]	
	α_a	6.2~9.7			5.8~9.2 [88]	
		6.6~10.4	_	_	8.3~11.9 [88]	
	$lpha_b \ C_p$	6.6~10.4 74~110	-	_	8.3~11.9 [88] 81~99 [82]	

During the simulations, the indenter moves down at a speed of 10 m/s. The time step is 1 fs. The simulations are performed at temperatures T=1, 300, 600, 900, 1200, and 1500 K. The indenter is initially 2 nm above the surface of TiB₂. At the beginning of each simulation, the whole system is relaxed for 10 ps at the desired temperature in the NVT ensemble, then the indenter moves down by 2.5 nm into the surface while the main part of the system is kept at NVE. The force of the indenter, P, is recorded during the simulation, and the contact pressure is calculated by H = P/A. A is the projected area of contact on the indentation plane and is calculated by $A = \pi \delta (2R - \delta)$, where δ is the indentation depth.

Fig. 4 shows the force of the indenter vs indentation depth for the simulation at 1 K. Initially, the material deforms elastically, and the force is increased smoothly as the indenter moves down. The first dislocation is observed at $\delta=1.3$ nm, where there is a sudden drop in the force. The currently available methods for automatic analysis of dislocations are limited to common crystal structures such as bcc, fcc, etc. [95], so we attempted to spot the dislocations visually. Fig. 5

includes snapshots of the indentation process at three different depths ($\delta = 0.5, 1.3, 1.75$ nm) in planes ($01\bar{1}0$) and ($\bar{1}2\bar{1}0$) as shown in Fig. 5(a).

It can be seen in Fig. 5(b) and (e) that at δ = 0.5 nm there is no change in the structure of TiB₂. At $\delta = 1.3$ nm (Fig. 5(c) and (f)), it is observed that a cone-shaped region is directly below the indenter. This region is gradually formed after the indentation depth passed 0.5 nm. A closer look at this region reveals that the titanium atoms still reside at their original positions in the lattice but the boron atoms have moved slightly away from their original positions and this has made a visually noticeable cone-shaped region. Although this region grows between δ = 0.5 nm and 1.3 nm, the indentation force follows its previous trend and has a smooth increase. Another observation at δ = 1.3 nm is the distinct vertical lines. These lines are caused by slip in the [0001] direction, which could be due to the slip of either the $\{10\overline{1}0\}$ or the $\{\bar{1}2\bar{1}0\}$ family of planes. In the literature, $\{10\bar{1}0\}$ has been assumed to be a possible slip plane in the [0001] direction for TiB2 since it has a wider planar distance [96]. For ZrB2, which has a similar crystal structure, both $\{10\bar{1}0\}$ and $\{\bar{1}2\bar{1}0\}$ have been suggested as possible slip planes in [0001] [97]. At $\delta = 1.75$ nm (Fig. 5(d) and Fig. 5(g)), we

Table 5

Comparison of the mechanical and physical properties of Ti₃B₄ and TiB-B_f calculated by MD, DFT, and experimental works.

		2NN-MEAM (This work)	DFT (This work)	Other DFT works	Experimental works
Γi ₃ Β ₄	а	3.22	3.26	3.258 [92]	3.260 [93]
	b	13.64	13.79	13.76 [92]	13.72 [93]
	c	3.01	3.04	3.041 [92]	3.041 [93]
	E_f	-0.91	-0.94	-0.94 [72], -0.933	_
	,			[75]	
	B	250	223	224.3 [81], 226 [75]	_
	E	450	487	488 [36]	394.4 529.9 [92]
	G	190	214	213 [36]	_
	ν	0.18	0.14	0.149 [36]	_
	C_{11}	442	412	420.3 [92], 415 [75]	_
	C_{22}	463	504	509.3 [92], 508 [75]	_
	C_{33}	541	576	576.5 [92], 578 [75]	_
	C_{44}	234	223	217.6 [92], 221 [75]	_
	C_{55}	216	241	222.2 [92], 239 [75]	_
	C_{66}	150	210	223.2 [92], 207 [75]	-
	C_{12}	132	116	113.9 [92], 114 [75]	_
	C_{13}	138	100	94.9 [92], 98 [75]	_
	C_{23}	70	52	50.0 [92], 52 [75]	-
$TiB-B_f$	a	3.20	3.29	3.283 [36]	3.27 [94]
	b	8.49	8.49	8.48 [36]	8.46 [94]
	c	3.01	3.05	3.051 [36]	3.05 [94]
	E_f	-0.79	-0.83	-0.814 [36]	-
	B	212	207	214 [36]	-
	E	401	438	438 [36]	-
	G	169	191	189 [36]	-
	ν	0.19	0.15	0.159 [36]	-
	C_{11}	398	405	409 [36], 409.5 [73]	-
	C_{22}	368	426	434 [36], 430.3 [73]	-
	C_{33}	474	516	521 [36], 520.2 [73]	-
	C_{44}	212	185	183 [36], 189.4 [73]	-
	C_{55}	186	229	229 [36], 230 [73]	-
	C_{66}	162	187	182 [36], 189 [73]	-
	C_{12}	135	110	121 [36], 104.3 [73]	-
	C_{13}	120	88	97 [36], 85.5 [73]	-
	C_{23}	86	62	65 [36], 56.7 [73]	_

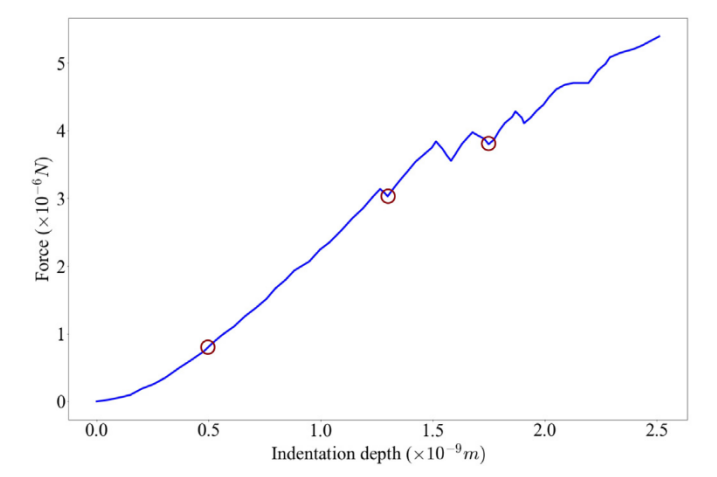


Fig. 4. Force vs. indentation depth of the simulation in 1 K. Snapshots of the simulation at the specified points in this figure are shown in Fig. 5.

see more dislocation lines in the [0001] direction, but no dislocation is detectable in the other directions. In addition, some parts of TiB_2 below the indenter are amorphized due to high pressure.

Fig. 6 shows the contact pressure of the indenter vs. indentation depth at different temperatures. The nanohardness of ${\rm TiB_2}$ at each temperature is calculated by averaging the value of the contact pressure between 1.5 nm and 2.5 nm where the pressure is stabilized. Fig. 7 shows the temperature dependence of the nanohardness of ${\rm TiB_2}$. As can be seen, there is a linear dependence between temperature and

nanohardness of ${\rm TiB}_2$ in the temperature range of $1{\sim}1500$ K. It shall be noted that all the available experimental measurements of nanohardness of ${\rm TiB}_2$ in the literature are done at room temperature. Based on different methods of production of ${\rm TiB}_2$, several values, such as 46.8 [20], 48.6 [16], 50 [19], 53 [98] and 57 and 73 GPa [21], are reported. In our simulation, the hardness at room temperature is 64 GPa, which falls in the range of experimental values. For ${\rm ZrB}_2$, which is a compound similar to ${\rm TiB}_2$, an experimental nanoindentation test has shown that there is about a 30% drop in nanohardness if the temperature is increased from room temperature to 600 °C [99]. In our simulation for the same temperature range, we obtained a 20% drop in nanohardness, which is reasonable. At 1500 K, our measured hardness is 43 GPa, which shows that ${\rm TiB}_2$ keeps its high hardness at elevated temperatures.

5. Conclusions

In this study, we developed a 2NN-MEAM potential for the Ti–B system. This potential reproduces the physical and mechanical properties of several titanium borides, including TiB, TiB $_2$, Ti $_3$ B $_4$, and TiB–B $_f$. It also predicts the thermal properties of TiB and TiB $_2$ very well. As an application of this potential, several nanoindentation simulations have been conducted to obtain the nanohardness of TiB2 in the [0001] direction at different temperatures. It was observed that dislocations occur due to plane slip in the [0001] direction. The calculated nanohardness of TiB $_2$ at room temperature is consistent with the reported experimental data. In addition, our results showed that there is a linear dependence between temperature and nanohardness of TiB $_2$ in the temperature range of 1~1500 K and that TiB $_2$ maintains a good hardness at temperatures up to 1500 K. The 2NN-MEAM potential

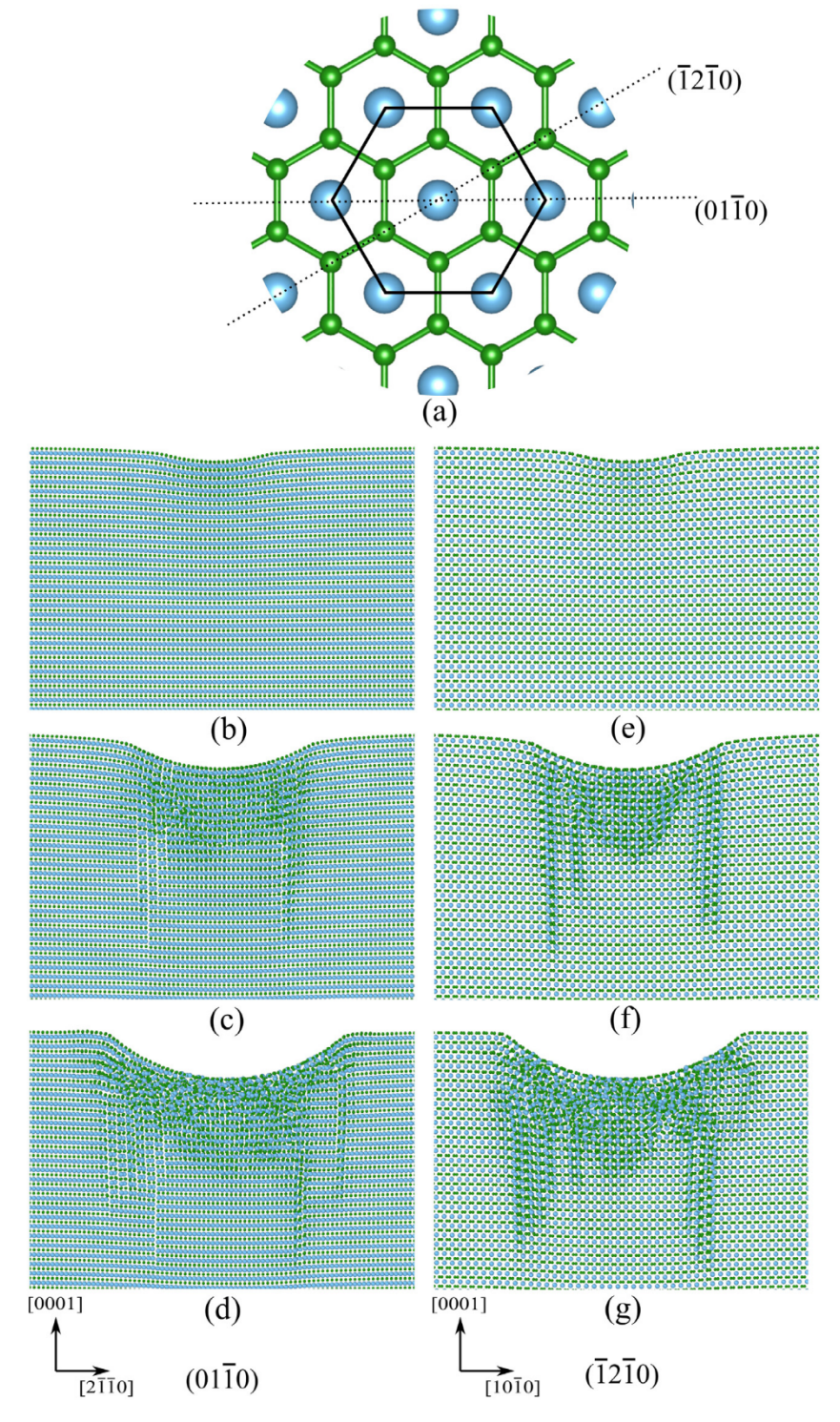


Fig. 5. (a) Crystal structure of TiB₂ from the [0001] direction; snapshots of the (01 $\bar{1}$ 0) plane at (b) $\delta = 0.5$ nm, (c) $\delta = 1.3$ nm, and (d) $\delta = 1.75$ nm; snapshots of plane ($\bar{1}2\bar{1}$ 0) at (e) $\delta = 0.5$ nm, (f) $\delta = 1.3$ nm, and (g) $\delta = 1.75$ nm.

developed in this paper is the first one available for studying the mechanics of titanium boride compounds.

CRediT authorship contribution statement

Siamak Attarian: Conceptualization, Methodology, Writing – original draft. **Shaoping Xiao:** Supervision, Reviewing and editing.

Declaration of competing interest

The authors declare that they have no known competing financial interests or personal relationships that could have appeared to influence the work reported in this paper.

Data availability

The LAMMPS input files used in this article are available from https://doi.org/10.17632/gy97bcv4dm.2.

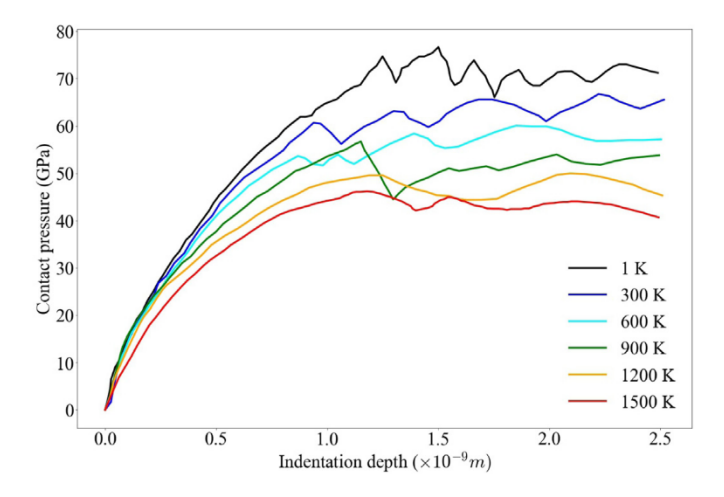


Fig. 6. Contact pressure vs. indentation depth for simulations at different temperatures.

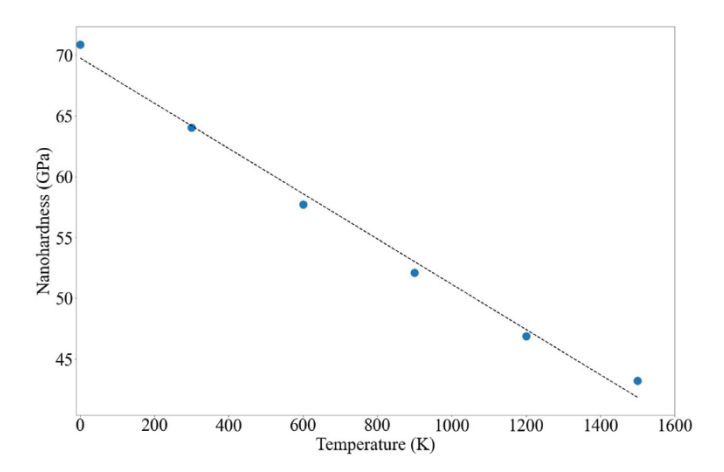


Fig. 7. Temperature dependence of nanohardness of TiB2 in the [0001] direction.

Acknowledgment

This material is based upon work supported by the National Science Foundation under Grant No. 2104383.

References

- Catherine Colinet, Jean Claude Tedenac, Enthalpies of formation of transition metal diborides: A first principles study, Crystals (ISSN: 20734352) 5 (4) (2015) 562–582, http://dx.doi.org/10.3390/cryst5040562.
- [2] K. Morsi, Review: titanium-titanium boride composites, J. Mater. Sci. 54 (9) (2019) 6753–6771, http://dx.doi.org/10.1007/s10853-018-03283-w.
- [3] Yang Du, Mingyin Kou, Jiguo Tu, Mingyong Wang, Shuqiang Jiao, An investigation into the anodic behavior of TiB2 in a CaCl2-based molten salt, Corros. Sci. (ISSN: 0010938X) 178 (October 2020) (2021) 1–7, http://dx.doi.org/10.1016/j.corsci.2020.109089.
- [4] J.L. Murray, P.K. Liao, K.E. Spear, The B-Ti (boron-titanium) system, Bull. Alloy Phase Diagr. (ISSN: 01970216) 7 (6) (1986) 550–555, http://dx.doi.org/10. 1007/BF02869864.
- [5] Takashi Saito, The automotive application of discontinuously reinforced TiB-Ti composites, Jom (ISSN: 10474838) 56 (5) (2004) 33–36, http://dx.doi.org/10. 1007/s11837-004-0125-3.
- [6] H. Attar, L. Löber, A. Funk, M. Calin, L.C. Zhang, K.G. Prashanth, S. Scudino, Y.S. Zhang, J. Eckert, Mechanical behavior of porous commercially pure Ti and Ti–TiB composite materials manufactured by selective laser melting, Mater. Sci. Eng. A (ISSN: 09215093) 625 (2015) 350–356, http://dx.doi.org/10.1016/j.msea.2014. 12.036.
- [7] S. Rodriguez, V.B. Munoz, V.E. Esquivel, L.E. Murr, N.L. Rupert, Microstructural characterization of TiB2 armor targets, J. Mater. Sci. Lett. (ISSN: 02618028) 21 (21) (2002) 1661–1666, http://dx.doi.org/10.1023/A:1020868524652.

- [8] Bin Zou, Chuanzhen Huang, Jinpeng Song, Ziye Liu, Lin Liu, Yan Zhao, Mechanical properties and microstructure of TiB 2-TiC composite ceramic cutting tool material, Int. J. Refract. Metals Hard Mater. (ISSN: 02634368) 35 (2012) 1–9, http://dx.doi.org/10.1016/j.ijrmhm.2012.02.011.
- [9] R.A. McDonald, Enthalpy, heat capacity, and heat of fusion of aluminum from 366° to 1647°K, J. Chem. Eng. Data (ISSN: 15205134) 12 (1) (1967) 115–118, http://dx.doi.org/10.1021/je60032a037.
- [10] S.C. Raj, M. Skyllas-Kazacos, Electrochemical studies on wettability of sintered TiB2 electrodes in aluminium electrolysis, Electrochim. Acta (ISSN: 00134686) 37 (8) (1992) 1395–1401, http://dx.doi.org/10.1016/0013-4686(92)87013-P.
- [11] Xiaoxiao Huang, Shuchen Sun, Ganfeng Tu, Investigation of mechanical properties and oxidation resistance of CVD TiB2 ceramic coating on molybdenum, J. Mater. Res. Technol. (ISSN: 22387854) 9 (1) (2020) 282–290, http://dx.doi.org/10.1016/j.jmrt.2019.10.056.
- [12] Balakrishnan Prakash, Christos Ftikos, Jean Pierre Celis, Fretting wear behavior of PVD TiB2 coatings, Surf. Coat. Technol. (ISSN: 02578972) 154 (2–3) (2002) 182–188, http://dx.doi.org/10.1016/S0257-8972(02)00035-X.
- [13] Martin Bohley, Sonja Kieren-Ehses, Lukas Heberger, Benjamin Kirsch, Jan C. Aurich, Size limitations and wear behavior of TiB2 coated micro end mills ($\phi < 50~\mu m$) when machining cp-titanium, Proc. CIRP 71 (2018) 187–191, http://dx.doi.org/10.1016/j.procir.2018.05.095.
- [14] P. Tatarko, S. Grasso, A. Kovalčíková, D. Medveď, I. Dlouhý, M.J. Reece, Highly textured and strongly anisotropic TiB2 ceramics prepared using magnetic field alignment (9T), J. Eur. Ceram. Soc. (ISSN: 1873619X) 40 (4) (2020) 1111–1118, http://dx.doi.org/10.1016/j.jeurceramsoc.2019.11.006.
- [15] M.N. Polyakov, M. Morstein, X. Maeder, T. Nelis, D. Lundin, J. Wehrs, J.P. Best, T.E.J. Edwards, M. Döbeli, J. Michler, Microstructure-driven strengthening of TiB 2 coatings deposited by pulsed magnetron sputtering, Surf. Coat. Technol. (ISSN: 02578972) 368 (November 2018) (2019) 88–96, http://dx.doi.org/10.1016/j. surfcoat.2019.04.042.
- [16] F. Lofaj, T. Moskalewicz, G. Cempura, M. Mikula, J. Dusza, A. Czyrska-Filemonowicz, Nanohardness and tribological properties of nc-TiB2 coatings, J. Eur. Ceram. Soc. (ISSN: 09552219) 33 (12) (2013) 2347–2353, http://dx.doi.org/10.1016/j.jeurceramsoc.2013.02.024.
- [17] I. Zyganitidis, N. Kalfagiannis, S. Logothetidis, Ultra sharp berkovich indenter used for nanoindentation studies of TiB2 thin films, Mater. Sci. Eng. B (ISSN: 09215107) 165 (3) (2009) 198–201, http://dx.doi.org/10.1016/j.mseb.2009.07. 016.
- [18] P.K.P. Rupa, P.C. Chakraborti, S.K. Mishra, Mechanical and deformation behaviour of titanium diboride thin films deposited by magnetron sputtering, Thin Solid Films (ISSN: 00406090) 517 (9) (2009) 2912–2919, http://dx.doi.org/10. 1016/j.tsf.2008.12.028.
- [19] Wei Dai, Tongjun Zhang, Junyou Yang, Rongxing Sun, Juliang Xu, Morphological analysis of TiB2 thin film prepared by rf magnetron sputtering, J. Vac. Sci. Technol. A: Vac. Surf. Films (ISSN: 0734-2101) 26 (4) (2008) 610–615, http: //dx.doi.org/10.1116/1.2943642.
- [20] N. Panich, P. Wangyao, S. Hannongbua, P. Sricharoenchai, Y. Sun, Nanoindentation and microscratch of annealed nanostructured TiB2 coatings, High Temp. Mater. Process. (ISSN: 03346455) 25 (5–6) (2006) 285–291, http://dx.doi.org/10.1515/HTMP.2006.25.5-6.285.
- [21] Marián Mikula, Branislav Grančič, Vilma Buršíková, Adrián Csuba, Milan Držík, Štefan Kavecký, Andrej Plecenik, Peter Kúš, Mechanical properties of superhard TiB2 coatings prepared by DC magnetron sputtering, Vacuum (ISSN: 0042207X) 82 (2 SPEC. ISS.) (2007) 278–281, http://dx.doi.org/10.1016/j.vacuum.2007.07. 036.
- [22] Saad Abdeslam, Results in Physics In fl uence of silver inclusions on the mechanical behavior of Cu-Ag nanocomposite during nanoindentation: Molecular dynamics study, Results Phys. (ISSN: 2211-3797) 15 (April) (2019) 102672, http://dx.doi.org/10.1016/j.rinp.2019.102672.
- [23] Henggao Xiang, Haitao Li, Jingjing Chen, Sha Sun, Qibin Li, Bo Yang, Xianghe Peng, Molecular dynamics simulation for orientation dependence of deformations in monocrystalline AlN during nanoindentation, Ceram. Int. (ISSN: 0272-8842) 44 (9) (2018) 10376–10382, http://dx.doi.org/10.1016/j.ceramint.2018.03.051.
- [24] Sandeep P. Patil, Vinayak G. Parale, Hyung-ho Park, Bernd Markert, Materials science & engineering a molecular dynamics and experimental studies of nanoin-dentation on nanoporous silica aerogels, Mater. Sci. Eng. A (ISSN: 0921-5093) 742 (November 2018) (2019) 344–352, http://dx.doi.org/10.1016/j.msea.2018. 11.019.
- [25] Junhua Zhao, Jin Wu Jiang, Timon Rabczuk, Temperature-dependent mechanical properties of single-layer molybdenum disulphide: Molecular dynamics nanoindentation simulations, Appl. Phys. Lett. (ISSN: 00036951) 103 (23) (2013) http://dx.doi.org/10.1063/1.4844935.
- [26] Chao Cheng, Yunli Ma, Qili Bao, Xun Wang, Jiaxing Sun, Gang Zhou, Hao Wang, Yanxia Liu, Dongsheng Xu, Development and application of EAM potentials for Ti, Al and Nb with enhanced planar fault energy of Ti, Comput. Mater. Sci. (ISSN: 09270256) 173 (December 2019) (2020) 109432, http://dx.doi.org/10.1016/j.commatsci.2019.109432.
- [27] Young-min Kim, Byeong-joo Lee, M.I. Baskes, Modified embedded-atom method interatomic potentials for Ti and Zr, Phys. Rev. B (2006) http://dx.doi.org/10. 1103/PhysRevB.74.014101.

- [28] Tao Liang, Michael Ashton, Kamal Choudhary, Difan Zhang, Alexandre F. Fonseca, Benjamin C. Revard, Richard G. Hennig, Simon R. Phillpot, Susan B. Sinnott, Properties of Ti/TiC interfaces from molecular dynamics simulations, J. Phys. Chem. C (ISSN: 19327455) 120 (23) (2016) 12530–12538, http://dx.doi.org/10.1021/acs.jpcc.6b02763.
- [29] Young Kwang Kim, Hong Kyu Kim, Woo Sang Jung, Byeong Joo Lee, Atomistic modeling of the Ti–Al binary system, Comput. Mater. Sci. (ISSN: 09270256) 119 (2016) 1–8, http://dx.doi.org/10.1016/j.commatsci.2016.03.038.
- [30] Varghese Swamy, Julian D. Gale, Transferable variable-charge interatomic potential for atomistic simulation of titanium oxides, Phys. Rev. B (ISSN: 01631829) 62 (9) (2000) 5406–5412. http://dx.doi.org/10.1103/PhysRevB.62.5406.
- [31] J.H. Los, J.M.H. Kroes, K. Albe, R.M. Gordillo, M.I. Katsnelson, A. Fasolino, Extended Tersoff potential for boron nitride: Energetics and elastic properties of pristine and defective h -BN, Phys. Rev. B (ISSN: 24699969) 96 (18) (2017) 1–11, http://dx.doi.org/10.1103/PhysRevB.96.184108.
- [32] Katsuyuki Matsunaga, Craig Fisher, Hideaki Matsubara, Tersoff potential parameters for simulating cubic boron carbonitrides, Japanese J. Appl. Phys. 2: Lett. (ISSN: 00214922) 39 (1 A/B) (2000) http://dx.doi.org/10.1143/jiap.39.148.
- [33] Won Ha Moon, Ho Jung Hwang, A modified stillinger-weber empirical potential for boron nitride, Appl. Surf. Sci. (ISSN: 01694332) 239 (3–4) (2005) 376–380, http://dx.doi.org/10.1016/j.apsusc.2004.05.284.
- [34] Siamak Attarian, Shaoping Xiao, Development of a 2NN-MEAM potential for boron, J. Micromech. Mol. Phys. 5 (3) (2020) 2050008, http://dx.doi.org/10. 1142/s2424913020500083.
- [35] Byeong-joo Lee, Hanchul Kim, Second nearest-neighbor modified embedded atom method potential for BCC transition metals, Phys. Rev. B 64 (October) (2001) http://dx.doi.org/10.1103/PhysRevB.64.184102, 184102 Second.
- [36] Pengfei Li, Rulong Zhou, Xiao Cheng Zeng, Computational analysis of stable hard structures in the Ti–B system, ACS Appl. Mater. Interfaces (ISSN: 19448252) 7 (28) (2015) 15607–15617, http://dx.doi.org/10.1021/acsami.5b04332.
- [37] Tao Liang, Tzu Ray Shan, Yu Ting Cheng, Bryce D. Devine, Mark Noordhoek, Yangzhong Li, Zhize Lu, Simon R. Phillpot, Susan B. Sinnott, Classical atomistic simulations of surfaces and heterogeneous interfaces with the charge-optimized many body (COMB) potentials, Mater. Sci. Eng. R: Rep. (ISSN: 0927796X) 74 (9) (2013) 255–279, http://dx.doi.org/10.1016/j.mser.2013.07.001.
- [38] Gang Liu, Hua Gui Yang, Chenghua Sun, Lina Cheng, Lianzhou Wang, Gao Qing Lu, Hui Ming Cheng, Titania polymorphs derived from crystalline titanium diboride, CrystEngComm (ISSN: 14668033) 11 (12) (2009) 2677–2682, http://dx.doi.org/10.1039/b909191m.
- [39] Young Min Kim, Byeong Joo Lee, Modified embedded-atom method interatomic potentials for the Ti-C and Ti-N binary systems, Acta Mater. (ISSN: 13596454) 56 (14) (2008) 3481–3489. http://dx.doi.org/10.1016/j.actamat.2008.03.027.
- [40] Eunkoo Lee, Kwang Ryeol Lee, M.I. Baskes, Byeong Joo Lee, A modified embedded-atom method interatomic potential for ionic systems: 2NN-MEAM+Qeq, Phys. Rev. B (ISSN: 24699969) 93 (14) (2016) 1–21, http://dx.doi.org/10.1103/PhysRevB.93.144110.
- [41] James H. Rose, John R. Smith, Francisco Guinea, John Ferrante, Universal features of the equation of state of metals, Phys. Rev. B (ISSN: 01631829) 29 (6) (1984) 2963–2969, http://dx.doi.org/10.1103/PhysRevB.29.2963.
- [42] M.I. Baskes, Modified embedded-atom potentials for cubic materials and impurities, Phys. Rev. B (ISSN: 01631829) 46 (5) (1992) 2727–2742, http://dx.doi.org/10.1103/PhysRevB.46.2727.
- [43] Rajan Khadka, Nirmal Baishnab, George Opletal, Ridwan Sakidja, Study of amorphous boron carbide (a-BxC) materials using molecular dynamics (MD) and hybrid reverse Monte Carlo (HRMC), J. Non-Crystall. Solids (ISSN: 00223093) 530 (October 2019) (2020) 119783, http://dx.doi.org/10.1016/j.jnoncrysol. 2019 119782
- [44] Bing Zheng, Hai Tao Yu, Yong Fu Lian, Ying Xie, Novel α- and β-type boron sheets: Theoretical insight into their structures, thermodynamic stability, and work functions, Chem. Phys. Lett. (ISSN: 00092614) 648 (2016) 81–86, http: //dx.doi.org/10.1016/j.cplett.2016.01.074.
- [45] Xiaojun Wu, Jun Dai, Yu Zhao, Zhiwen Zhuo, Jinlong Yang, Xiao Cheng Zeng, Two-dimensional boron monolayer sheets, ACS Nano (ISSN: 19360851) 6 (8) (2012) 7443–7453, http://dx.doi.org/10.1021/nn302696v.
- [46] Nevill Gonzalez Szwacki, Arta Sadrzadeh, Boris I. Yakobson, B80 fullerene: An ab initio prediction of geometry, stability, and electronic structure, Phys. Rev. Lett. (ISSN: 00319007) 98 (16) (2007) 1–4, http://dx.doi.org/10.1103/PhysRevLett. 98.166804.
- [47] Mary Anne White, Anthony B. Cerqueira, Catherine A. Whitman, Michel B. Johnson, Tadashi Ogitsu, Determination of phase stability of elemental boron, Angew. Chem. 127 (12) (2015) 3697–3700, http://dx.doi.org/10.1002/ange. 201409169
- [48] Swagata Roy, Amlan Dutta, Nirupam Chakraborti, A novel method of determining interatomic potential for Al and Al-Li alloys and studying strength of Al-Al3Li interphase using evolutionary algorithms, Comput. Mater. Sci. (ISSN: 0927-0256) 190 (2021) 110258, http://dx.doi.org/10.1016/j.commatsci.2020.110258.
- [49] David H. Wolpert, William G. Macready, No free lunch theorems for optimization, IEEE Trans. Evol. Comput. 1 (1) (1997) 67–82, http://dx.doi.org/10.1109/ 4235.585893.

- [50] Kalyanmoy Deb, Samir Agrawal, Amrit Pratap, Tanaka Meyarivan, A fast elitist non-dominated sorting genetic algorithm for multi-objective optimization: NSGA-II.
- [51] James Kennedy, Russell Eberhart, Particle swarm optimization, http://dx.doi.org/ 10.1109/ICNN.1995.488968
- [52] Jun Sun, Bin Feng, Wenbo Xu, Particle swarm optimization with particles having quantum behavior, http://dx.doi.org/10.1109/CEC.2004.1330875.
- [53] Seyedali Mirjalili, Seyed Mohammad Mirjalili, Andrew Lewis, Grey wolf optimizer, http://dx.doi.org/10.1016/j.advengsoft.2013.12.007.
- [54] Xin-She Yang, Firefly algorithm, stochastic test functions and design optimisation, http://dx.doi.org/10.1504/IJBIC.2010.032124.
- [55] Nikolaus Hansen, Sibylle D. Müller, Petros Koumoutsakos, Reducing the time complexity of the derandomized evolution strategy with covariance matrix adaptation (CMA-ES), http://dx.doi.org/10.1162/106365603321828970.
- [56] Shoubing Ding, Xinqiang Wang, A systematic study on the MEAM interatomic potentials of the transition metal nitrides TMNs (TM=Ti, V, Cr, Fe) binary systems, J. Alloys Compd. (ISSN: 09258388) 805 (2019) 1081–1089, http://dx. doi.org/10.1016/j.jallcom.2019.07.114.
- [57] Amir Karton, Jan M.L. Martin, Heats of formation of beryllium, boron, aluminum, and silicon re-examined by means of W4 theory, J. Phys. Chem. A (ISSN: 10895639) 111 (26) (2007) 5936–5944, http://dx.doi.org/10.1021/jp071690x.
- [58] Paolo Giannozzi, Stefano Baroni, Nicola Bonini, Matteo Calandra, Roberto Car, Carlo Cavazzoni, Davide Ceresoli, Guido L. Chiarotti, Matteo Cococcioni, Ismaila Dabo, Andrea Dal Corso, Stefano De Gironcoli, Stefano Fabris, Guido Fratesi, Ralph Gebauer, Uwe Gerstmann, Christos Gougoussis, Anton Kokalj, Michele Lazzeri, Layla Martin-Samos, Nicola Marzari, Francesco Mauri, Riccardo Mazzarello, Stefano Paolini, Alfredo Pasquarello, Lorenzo Paulatto, Carlo Sbraccia, Sandro Scandolo, Gabriele Sclauzero, Ari P. Seitsonen, Alexander Smogunov, Paolo Umari, Renata M. Wentzcovitch, QUANTUM ESPRESSO: A modular and open-source software project for quantum simulations of materials, J. Phys. Condens. Matter (ISSN: 09538984) 21 (39) (2009) http://dx.doi.org/10.1088/0953-8984/21/39/395502.
- [59] P.E. Blöchl, Projector augmented-wave method, Phys. Rev. B (ISSN: 01631829) 50 (24) (1994) 17953–17979, http://dx.doi.org/10.1103/PhysRevB.50.17953.
- [60] John P. Perdew, Kieron Burke, Matthias Ernzerhof, Generalized gradient approximation made simple, Phys. Rev. Lett. 77 (3) (1996) 3865–3868.
- [61] Won-seok Ko, Blazej Grabowski, Development and application of a Ni-Ti interatomic potential with high predictive accuracy of the martensitic phase transition, Phys. Rev. B 134107 (2015) 1–22, http://dx.doi.org/10.1103/PhysRevB. 92.134107
- [62] Jackelyn A. Martinez, Dundar E. Yilmaz, Tao Liang, Susan B. Sinnott, Simon R. Phillpot, Fitting empirical potentials: Challenges and methodologies, Curr. Opin. Solid State Mater. Sci. (ISSN: 13590286) 17 (6) (2013) 263–270, http://dx.doi.org/10.1016/j.cossms.2013.09.001.
- [63] Steve Plimpton, Short-range molecular dynamics, J. Comput. Phys. (ISSN: 00219991) 117 (6) (1997) 1–42, http://dx.doi.org/10.1006/jcph.1995.1039.
- [64] Koichi Momma, Fujio Izumi, VESTA 3 for three-dimensional visualization of crystal, volumetric and morphology data, J. Appl. Crystallogr. (ISSN: 00218898) 44 (6) (2011) 1272–1276, http://dx.doi.org/10.1107/S0021889811038970.
- [65] Alexander Stukowski, Visualization and analysis of atomistic simulation data with OVITO-the Open Visualization Tool, Modelling Simulation Mater. Sci. Eng. (ISSN: 09650393) 18 (1) (2010) http://dx.doi.org/10.1088/0965-0393/18/1/015012.
- [66] Francis Birch, Finite elastic strain of cubic crystals, Phys. Rev. (ISSN: 0031899X) 71 (11) (1947) 809–824, http://dx.doi.org/10.1103/PhysRev.71.809.
- [67] R. Hill, The elastic behaviour of a crystalline aggregate, Proc. Phys. Soc. A (ISSN: 03701298) 65 (5) (1952) 349–354, http://dx.doi.org/10.1088/0370-1298/65/5/207
- [68] Lili Liu, Xiaozhi Wu, Rui Wang, Xiangfei Nie, Yelu He, Xing Zou, First-principles investigations on structural and elastic properties of orthorhombic TiAl under pressure, Crystals (ISSN: 20734352) 7 (4) (2017) http://dx.doi.org/10.3390/ cryst7040111.
- [69] J.E. Turney, A.J.H. McGaughey, C.H. Amon, Assessing the applicability of quantum corrections to classical thermal conductivity predictions, Phys. Rev. B (ISSN: 10980121) 79 (22) (2009) 1–7, http://dx.doi.org/10.1103/PhysRevB.79. 224305
- [70] A.J.H. McGaughey, M. Kaviany, Quantitative validation of the Boltzmann transport equation phonon thermal conductivity model under the single-mode relaxation time approximation, Phys. Rev. B (ISSN: 01631829) 69 (9) (2004) 943031–9430312, http://dx.doi.org/10.1103/PhysRevB.69.094303.
- [71] C.Z. Wang, C.T. Chan, K.M. Ho, Empirical tight-binding force model for molecular-dynamics simulation of si, Phys. Rev. B (ISSN: 01631829) 39 (12) (1989) 8586–8592, http://dx.doi.org/10.1103/PhysRevB.39.8586.
- [72] Liang Sun, Yimin Gao, Bing Xiao, Yefei Li, Guoliang Wang, Anisotropic elastic and thermal properties of titanium borides by first-principles calculations, J. Alloys Compd. (ISSN: 09258388) 579 (2013) 457–467, http://dx.doi.org/10. 1016/j.jallcom.2013.06.119.
- [73] Bo Huang, Yong Hua Duan, Wen Cheng Hu, Yong Sun, Shuai Chen, Structural, anisotropic elastic and thermal properties of MB (M=Ti, Zr and Hf) monoborides, Ceram. Int. (ISSN: 02728842) 41 (5) (2015) 6831–6843, http://dx.doi.org/10.1016/j.ceramint.2015.01.132.

- [74] B.F. Decker, J.S. Kasper, The crystal structure of TiB, Acta Crystal-logr. (ISSN: 0365-110X) 7 (1) (1954) 77–80, http://dx.doi.org/10.1107/s0365110x5400014x.
- [75] Maarten De Jong, Wei Chen, Thomas Angsten, Anubhav Jain, Randy Notestine, Anthony Gamst, Marcel Sluiter, Chaitanya Krishna Ande, Sybrand Van Der Zwaag, Jose J. Plata, Cormac Toher, Stefano Curtarolo, Gerbrand Ceder, Kristin A. Persson, Mark Asta, Charting the complete elastic properties of inorganic crystalline compounds, Sci. Data (ISSN: 20524463) 2 (2015) 1–13, http://dx.doi.org/10.1038/sdata.2015.9.
- [76] L.I. Yan-feng, X.U. Hui, X.I.A. Qing-lin, LIU Xiao-liang, First-principles calculation of structural and thermodynamic properties of titanium boride, J. Cent. South Univ. Technol. 18 (2011) 1173–1779, http://dx.doi.org/10.1007/s11771-011-0901-5.
- [77] K.B. Panda, K.S.Ravi Chandran, First principles determination of elastic constants and chemical bonding of titanium boride (TiB) on the basis of density functional theory, Acta Mater. (ISSN: 13596454) 54 (6) (2006) 1641–1657, http://dx.doi. org/10.1016/j.actamat.2005.12.003.
- [78] R.R. Atri, K.S. Ravichandran, S.K. Jha, Elastic properties of in-situ processed Ti–TiB composites measured by impulse excitation of vibration, Mater. Sci. Eng. A (ISSN: 09215093) 271 (1–2) (1999) 150–159, http://dx.doi.org/10.1016/ s0921-5093(99)00198-7.
- [79] Guojian Cao, Lin Geng, Masaaki Naka, Elastic properties of titanium monoboride measured by nanoindentation, J. Am. Ceram. Soc. (ISSN: 00027820) 89 (12) (2006) 3836–3838, http://dx.doi.org/10.1111/j.1551-2916.2006.01280.x.
- [80] G. Constantinides, K.S. Ravi Chandran, F.J. Ulm, K.J. Van Vliet, Grid indentation analysis of composite microstructure and mechanics: Principles and validation, Mater. Sci. Eng. A (ISSN: 09215093) 430 (1–2) (2006) 189–202, http://dx.doi. org/10.1016/j.msea.2006.05.125.
- [81] Peeyush Nandwana, Niraj Gupta, Srivilliputhur G. Srinivasan, Rajarshi Banerjee, A first principles study of commonly observed planar defects in Ti/TiB system, Comput. Mater. Sci. (ISSN: 09270256) 150 (August 2017) (2018) 197–201, http://dx.doi.org/10.1016/j.commatsci.2018.04.006.
- [82] Malcolm W. Chase, NIST-JANAF Thermochemical tables, 4th ed. J. Phys. Chem. Ref. Data. 1998, monograph 9(part I and part II), J. Phys. Chem. Ref. Data Monograph (1998) Part I&II.
- [83] D. Galvan, V. Ocelı, Y. Pei, B.J. Kooi, De Jeff Th M. Hosson, E. Ramous, Microstructure and properties of TiB/Ti-6Al-4V coatings produced with laser treatments, J. Mater. Eng. Perform. 13 (August) (2004) 406–412, http://dx.doi. org/10.1361/10599490419919.
- [84] Norihiko L. Okamoto, Misato Kusakari, Katsushi Tanaka, Haruyuki Inui, Shigeki Otani, Anisotropic elastic constants and thermal expansivities in monocrystal CrB2, TiB2, and ZrB2, Acta Mater. (ISSN: 13596454) 58 (1) (2010) 76–84, http://dx.doi.org/10.1016/j.actamat.2009.08.058.
- [85] Ashish Jain, R. Pankajavalli, S. Anthonysamy, K. Ananthasivan, R. Babu, V. Ganesan, G.S. Gupta, Determination of the thermodynamic stability of TiB2, J. Alloys Compd. (ISSN: 09258388) 491 (1–2) (2010) 747–752, http://dx.doi.org/10.1016/j.jallcom.2009.11.058.
- [86] R.G. Munro, Material properties of titanium diboride, Elsevier Appl. Sci. (ISSN: 1044-677X) 105 (5) (2000) 709, http://dx.doi.org/10.6028/jres.105.057.
- [87] P.S. Spoor, J.D. Maynard, M.J. Pan, D.J. Green, J.R. Hellmann, T. Tanaka, Elastic constants and crystal anisotropy of titanium diboride, Appl. Phys. Lett. (ISSN: 00036951) 70 (15) (1997) 1959–1961, http://dx.doi.org/10.1063/1.118791.

- [88] E. Fendler, O. Babushkin, T. Lindback, R. Telle, G. Petzow, Thermal expansion of diboride solid solutions, in: R. Carlsson, T. Johansson, L. Kahlman (Eds.), 4th International Symposium on Ceramic Materials and Components for Engines, Springer, Dordrecht, 1992, pp. 204–212, http://dx.doi.org/10.1007/978-94-011-2882-7 16 (ISSN: 0302072X)
- [89] Hai Yan Yan, Qun Wei, Shao Mei Chang, Ping Guo, A first-principle calculation of structural, mechanical and electronic properties of titanium borides, Trans. Nonferr. Metals Soc. China (Engl. Ed.) (ISSN: 10036326) 21 (7) (2011) 1627–1633, http://dx.doi.org/10.1016/S1003-6326(11)60906-0.
- [90] Nils Nedfors, Oleksiy Vozniy, Johanna Rosen, Effect of synchronized bias in the deposition of TiB 2 thin films using high power impulse magnetron sputtering, J. Vac. Sci. Technol. A: Vac. Surf. Films (ISSN: 0734-2101) 36 (3) (2018) 031510, http://dx.doi.org/10.1116/1.5003194.
- [91] Yangzhong Li, Anuj Goyal, Aleksandr Chernatynskiy, Jay S. Jayashankar, Michael C. Kautzky, Susan B. Sinnott, Simon R. Phillpot, Nanoindentation of gold and gold alloys by molecular dynamics simulation, Mater. Sci. Eng. A (ISSN: 09215093) 651 (2016) 346–357, http://dx.doi.org/10.1016/j.msea.2015.10.081.
- [92] Somnaang Rou, K.S.Ravi Chandran, First principles calculation of single-crystal elastic constants of titanium tetraboride (Ti3B4) and experimental validation, J. Am. Ceram. Soc. (ISSN: 15512916) 101 (9) (2018) 4308–4320, http://dx.doi. org/10.1111/jace.15562.
- [93] Karl E. Spear, Penny Mcdowell, Francis Mcmahon, Experimental evidence for the existence of the Ti3B4 phase, J. Am. Ceram. Soc. (ISSN: 15512916) 69 (1) (1986) C-4-C-5, http://dx.doi.org/10.1111/j.1151-2916.1986.tb04701.x.
- [94] Ludovic Ropars, Moukrane Dehmas, Sophie Gourdet, Jérôme Delfosse, David Tricker, Elisabeth Aeby-Gautier, Structure evolutions in a Ti-6Al-4V matrix composite reinforced with TiB, characterised using high energy X-ray diffraction, J. Alloys Compd. (ISSN: 09258388) 624 (2015) 179–188, http://dx.doi.org/10. 1016/j.jallcom.2014.10.203, URL http://dx.doi.org/10.1016/j.jallcom.2014.10. 203
- [95] Alexander Stukowski, Dislocation analysis tool for atomistic simulations, in: Handbook of Materials Modeling, 2020, pp. 1545–1558, http://dx.doi.org/10. 1007/978-3-319-44677-6 20.
- [96] Jeffrey R. Ramberg, Wendell S. Williams, High temperature deformation of titanium diboride, J. Mater. Sci. (ISSN: 00222461) 22 (5) (1987) 1815–1826, http://dx.doi.org/10.1007/BF01132411.
- [97] Dipankar Ghosh, Ghatu Subhash, Gerald R. Bourne, Room-temperature dislocation activity during mechanical deformation of polycrystalline ultra-high-temperature ceramics, Scr. Mater. (ISSN: 13596462) 61 (11) (2009) 1075–1078, http://dx.doi.org/10.1016/j.scriptamat.2009.08.038, URL http://dx.doi.org/10.1016/j.scriptamat.2009.08.038.
- [98] Teng Fei Zhang, Bin Gan, Seong mo Park, Qi Min Wang, Kwang Ho Kim, Influence of negative bias voltage and deposition temperature on microstructure and properties of superhard TiB2 coatings deposited by high power impulse magnetron sputtering, Surf. Coat. Technol. (ISSN: 02578972) 253 (2014) 115– 122, http://dx.doi.org/10.1016/j.surfcoat.2014.05.023, URL http://dx.doi.org/ 10.1016/j.surfcoat.2014.05.023.
- [99] Esteban Broitman, Lina Tengdelius, Ude D. Hangen, Jun Lu, Lars Hultman, Hans Högberg, High-temperature nanoindentation of epitaxial ZrB2 thin films, Scr. Mater. (ISSN: 13596462) 124 (2016) 117–120, http://dx.doi.org/10.1016/ j.scriptamat.2016.06.033.